

STELLAR AND PLANETARY PROPERTIES OF K2 CAMPAIGN 1 CANDIDATES AND VALIDATION OF 18 SYSTEMS, INCLUDING A PLANET RECEIVING EARTH-LIKE INSOLATION

BENJAMIN T. MONTET^{1,2}, TIMOTHY D. MORTON³, DANIEL FOREMAN-MACKEY^{4,5}, JOHN ASHER JOHNSON²,
DAVID W. HOGG^{4,6,5}, BRENDAN P. BOWLER^{1,7}, DAVID W. LATHAM², ALLYSON BIERYLA², ANDREW W. MANN^{8,9},(Dated: Sunday 2nd September, 2018, 06:10)*Draft version Sunday 2nd September, 2018*

ABSTRACT

The extended *Kepler* mission, *K2*, is now providing photometry of new fields every three months in a search for transiting planets. In a recent study, Foreman-Mackey and collaborators presented a list of 36 planet candidates orbiting 31 stars in *K2* Campaign 1. In this contribution, we present stellar and planetary properties for all systems. We combine ground-based seeing-limited survey data and adaptive optics imaging with an automated transit analysis scheme to validate 18 candidates as planets and identify 6 candidates as likely false positives. Of particular interest is EPIC 201912552, a bright ($K=8.9$) M2 dwarf hosting a $2.24 \pm 0.25 R_{\odot}$ planet with $T_{eq} = 271 \pm 16$ K and an orbital period of 33 days. We also present two new open-source software packages that enabled this analysis: **isochrones**, a flexible tool for fitting theoretical stellar models to observational data to determine stellar properties, and **vespa**, a new general-purpose procedure to calculate false positive probabilities and statistically validate transiting exoplanets.

Subject headings: catalogs — planetary systems — planets and satellites: detection — stars: fundamental parameters

1. INTRODUCTION

The *Kepler* telescope (Borucki et al. 2010) has led to a revolution in stellar and planetary astrophysics, with 7305 “objects of interest” and 4173 “planet candidates” discovered to date (Borucki et al. 2011a,b; Batalha et al. 2013; Burke et al. 2014; Rowe et al. 2015; Mullally et al. 2015). The fidelity of this sample is high: most of these planet candidates are truly planets (Morton & Johnson 2011; Fressin et al. 2013; Désert et al. 2015). The mechanical failure of two reaction wheels on the spacecraft led to a repurposing of the spacecraft into the *K2* mission, in which the telescope points at fields near the ecliptic plane for ~ 75 days at a time (Howell et al. 2014). In this observing strategy, two axes of motion of the spacecraft are controlled by the two remaining reaction wheels, while the roll of the spacecraft is balanced with solar radiation pressure and quasiperiodic thruster firing. As a result, the detector drifts relative to the sky at the rate of $\sim 1'' \text{ hr}^{-1}$, with rapid corrections due to thruster fires approximately once every six hours. Over the full duration of each campaign, the targets appear to remain

near the same location on the detector but both the slow drift and the corrections are observable by eye (Barentsen 2015).

K2 light curves produced with aperture photometry contain substantial pointing-induced photometric variations caused by the star’s apparent motion over a poorly-defined flat field. Worse yet, these variations occur on timescales similar to transit signals, potentially masking the observational signature of a planet passing between *Kepler* and its host star.

There has been considerable effort to recover these planetary signals, and to date six planets have been confirmed orbiting three stars in the *K2* data (Vanderburg et al. 2015; Crossfield et al. 2015; Armstrong et al. 2015b). What is common to all of these methods are that removal of systematics is considered a step to be undertaken before the search for planets. Under this strategy, it is implicitly assumed that the systematics are removed perfectly, while retaining all of the astrophysical signal. Of course, it is impossible to perfectly separate the astrophysical and instrumental signal, and such a technique is prone to either over-fitting, in which some of the astrophysical signal is also removed, or under-fitting, in which some of the instrumental systematics remain. A better strategy is to simultaneously fit both the signal and the systematics, as is common practice in cosmology and, increasingly, in radial velocity searches for planetary systems (e.g. Ferreira & Jaffe 2000; Boisse et al. 2011; Haywood et al. 2014; Grunblatt et al. 2015).

Foreman-Mackey et al. (2015) simultaneously fit both the systematics and potential planetary transit signals in a search for transiting planets. They assume that the dominant trends in the observed stellar light curves are caused by spacecraft motion and are shared by many stars. They then run PCA on all stars to measure the dominant modes, modeling each star as a linear combi-

btm@astro.caltech.edu

¹ Cahill Center for Astronomy and Astrophysics, California Institute of Technology, Pasadena, CA, 91125, USA² Harvard-Smithsonian Center for Astrophysics, Cambridge, MA 02138, USA³ Department of Astrophysics, Princeton University, Princeton, NJ, 08544, USA⁴ Center for Cosmology and Particle Physics, Department of Physics, New York University, 4 Washington Place, New York, NY, 10003, USA⁵ Center for Data Science, New York University, 726 Broadway, 7th Floor, New York, NY, 10003, USA⁶ Max-Planck-Institut für Astronomie, Königstuhl 17, D-69117 Heidelberg, Germany⁷ Caltech Joint Center for Planetary Astronomy Fellow⁸ Department of Astronomy, The University of Texas at Austin, Austin, TX 78712, USA⁹ Harlan J. Smith Fellow, The University of Texas at Austin

nation of 150 of these “eigen light curves” and a transit signal. This method enables fitting without over-fitting, and also permits marginalization over uncertainties induced by the systematic model. Therefore, any uncertainties in the systematics can be propagated into uncertainties in detected planet parameters, instead of assuming the systematics are understood perfectly. Using this technique, Foreman-Mackey et al. (2015) detect 36 planet candidates orbiting 31 stars in *K2* Campaign 1 data.

In Foreman-Mackey et al. (2015), only transit properties are provided, not absolute parameters about the planet or the star. Additionally, the authors follow the convention of the *Kepler* team to include any transit event as a candidate system rather than a false positive if a secondary eclipse is not detected: there is no enforced upper limit on the allowed planet radius. The authors intentionally make no effort to separate true transiting planets from astrophysical events that mimic the appearance of transits, such as an eclipsing binary with a high mass ratio, similar to the *Kepler* team’s list of “objects of interest.”

In this paper, we present stellar and planetary parameters for each system. We also analyze the false positive probability of each system using *vespa*, a new publicly available, general-purpose implementation of the Morton (2012) procedure to calculate false positive probabilities (FPPs) for transiting planets. Through this analysis, as well as archival imaging, ground-based seeing-limited survey data, and adaptive optics imaging, we are able to confirm 18 of these systems as transiting planets at the 99% confidence level. Additionally, we identify six systems as false positives.

This paper is organized as follows. In §2, we develop stellar properties through photometric and spectroscopic data. In §3, we combine the derived stellar properties with *K2* data to infer planet candidate properties. In §4, we combine adaptive optics and radial velocity observations with both archival and modern ground-based, seeing limited survey data and an analysis of the transit parameters to calculate false positive probabilities. In §5, we discuss potentially interesting systems, including a mini-Neptune orbiting an M dwarf which receives a similar insolation to the Earth. In §6, we summarize and discuss our results.

2. STELLAR PROPERTIES

2.1. Photometry

With the exception of one star in our sample (EPIC 201912552), we do not have spectroscopic data with which to characterize the stellar properties. Additionally, there are no measured parallaxes for any of these stars. Instead, we rely on photometry. For each system, we query the VizieR database of astronomical catalogues (Ochsenbein et al. 2000). We record the B , V , g' , r' , and i' magnitudes and their uncertainties from the AAVSO Photometric all-sky survey (APASS) DR6 (Henden & Munari 2014), as reported in the UCAC4 Catalogue (Zacharias et al. 2012). We also record the J , H , and K magnitudes and their uncertainties as found in the 2MASS All-Sky Catalog of Point Sources (Cutri et al. 2003) and the $W1 - W3$ WISE magnitudes and uncertainties from the ALLWISE Data Release (Cutri &

et al. 2013). For all except two of our targets, the $W4$ band is only an upper limit, and in the remaining two cases, the photometric uncertainty in $W4$ is at least an order of magnitude larger than those in $W1 - W3$, so we do not use $W4$ for any system. These data are reported in Table 1, and a color-color diagram showing the $r - J$, $J - K$ colors of our candidates is included as Fig. 1.

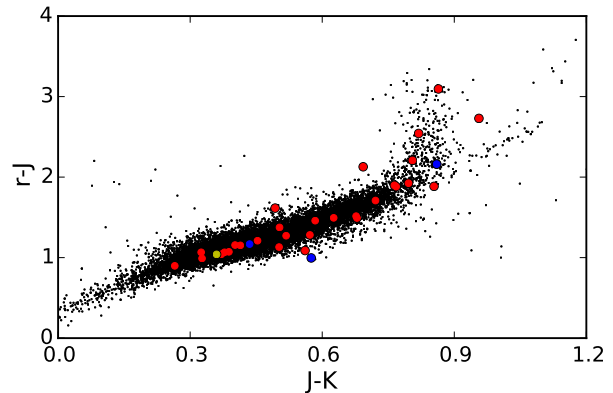


FIG. 1.— Color-color diagram displaying $r - J$, $J - K$ photometry for targets observed by *Kepler* during the original mission (black), with our *K2* Campaign 1 planet candidates overlaid (red). Also included is the location of the Sun (yellow) and host stars of previously confirmed *K2* planets (blue). 90% of our candidates have photometry consistent with later spectral types than the Sun.

2.2. Stellar Models

To convert the observed photometric data into physical properties for each star, we used the new publicly available *isochrones* Python module¹⁰, a general-purpose interpolation tool for the fitting of stellar models to photometric or spectroscopic parameters. This software does trilinear interpolation in mass–age– $[\text{Fe}/\text{H}]$ space for any given set of model grids, thus being able to predict the value for any physical or photometric property provided by the models at any values of mass, age, and $[\text{Fe}/\text{H}]$ within the boundaries of the grid.

This enables a set of observed properties ($\{x_i, \sigma_i\}$), either spectroscopic, photometric, or both, to define a likelihood function that may be sampled in an MCMC chain:

$$\ln \mathcal{L}(\theta) \propto -\frac{1}{2} \sum_i \frac{(x_i - I_i(\theta))^2}{\sigma_i^2}, \quad (1)$$

where $I_i(\theta)$ is the isochrone model prediction of property i at the given parameters θ . If the observed properties include any apparent magnitudes, then θ includes distance and extinction in addition to mass, age, and $[\text{Fe}/\text{H}]$.

In this work, we use grids from the Dartmouth Stellar Evolution Database (Dotter et al. 2008) at solar values of $[\alpha/\text{Fe}] = 0.0$ and helium abundance $Y = 0.2741$, which come packaged with the *isochrones* module. We then run an MCMC chain using *emcee* (Foreman-Mackey et al. 2013), an implementation of the affine-invariant ensemble sampler of Goodman & Weare (2010) for each host star conditioned on the observed photometric properties as presented in Table 1. We include a prior on stel-

¹⁰ <http://github.com/timothymorton/isochrones>

lar metallicity representative of the observed metallicities of stars within 1 kpc of the Sun, following the results of Hayden et al. (2015), and a Salpeter-slope prior on mass (up to the maximum mass available in the model grids of $3.7 M_{\odot}$).

Such a scheme enables us to infer the statistical uncertainties on the mass, radius, and effective temperature. However, we are subject to biases induced by systematics in the models themselves. There is some evidence that the Dartmouth models may under-predict radii of M dwarfs by $\sim 15\%$ when compared to other methods (Newton et al. 2015; Montet et al. 2015). Such an effect may be the result of the Dartmouth model reliance on BT-Settl atmospheres, which are based on incomplete molecular line lists and have been shown to predict near-IR colors that are too blue (Thompson et al. 2014).

In order to account for the effects of model uncertainties, we also run MCMC chains with photometric errors inflated artificially by a factor of three. The observed photometric parameters are then consistent with spectroscopically-derived parameters for stars with published spectra, and consistent with typical uncertainties from photometric data (e.g. Huber et al. 2014). We provide full chains using both inflated and un-inflated uncertainties,¹¹ though in the rest of this work (and in Table 2) we adopt the results obtained using the inflated values.

2.3. SNIFS and SpeX Spectroscopy

A near-infrared spectrum of EPIC 201912552 was obtained using the upgraded SpeX (uSpeX) spectrograph (Rayner et al. 2003) on the NASA Infrared Telescope Facility (IRTF) on January 29 2015 (UT). SpeX observations were taking using the short cross-dispersed mode and the $0.3 \times 15''$ slit, which provides simultaneous coverage from 0.7 to $2.5 \mu\text{m}$ at $R \simeq 2000$. The target was observed at two positions along the slit to subsequently subtract the sky background. Eight spectra were taking following this pattern, which provided a final S/N of > 150 per resolving element. The spectrum was flat fielded, extracted, wavelength calibrated, and stacked using the *Spectool* package (Cushing et al. 2004). An A0V-type star was observed immediately after the target, which was used to create a telluric correction using the *xtellcor* package (Vacca et al. 2003).

An optical spectrum was obtained using the SuperNova Integral Field Spectrograph (SNIFS, Aldering et al. 2002; Lantz et al. 2004) on the University of Hawai'i 2.2m telescope on the night of January 30 2015. SNIFS provides simultaneous coverage from 3200\AA – 9700\AA at a resolution of $\simeq 1000$. Final S/N of the spectrum was > 100 per resolving element in the red ($\sim 6000\text{\AA}$). Details of the SNIFS reduction, including dark, bias, and flat-field corrections, cleaning the data of bad pixels and cosmic rays, and extraction of the one-dimensional spectrum are described in Bacon et al. (2001) and Aldering et al. (2006). Flux calibration was performed using a separate pipeline described in Mann et al. (2015).

T_{eff} was calculated by comparing our optical spectra with the CFIST suite¹² of the BT-SETTL version of the PHOENIX atmosphere models (Allard et al. 2013), which gave a temperature of 3503 ± 60 K. More details

of this procedure are given in Mann et al. (2013b) and Gaidos et al. (2014). This method was used because it is known to accurately reproduce empirical T_{eff} values from long-baseline optical interferometry Boyajian et al. (2012).

Metallicity was determined using the procedures from Mann et al. (2013a), in which the authors provide empirical relations between atomic features and M dwarf metallicity, calibrated using wide binaries. We adopted the weighted mean of the H – and K –band calibrations, which yielded a metallicity of 0.09 ± 0.09 .

We combined the derived T_{eff} and $[\text{Fe}/\text{H}]$ values with the empirical $T_{\text{eff}}\text{--}[\text{Fe}/\text{H}]\text{--}R_*$ relation from Mann et al. (2015) to compute a radius. Accounting for measurement and calibration errors in $[\text{Fe}/\text{H}]$ and T_{eff} we calculated a radius $0.394 \pm 0.038 R_{\odot}$. We use these parameters instead of the derived photometric properties for this target.

The full list of stellar parameters adopted in this paper is included in Table 2.

3. PLANET PROPERTIES

In Foreman-Mackey et al. (2015), only parameters directly observable from the $K2$ light curve itself were reported: the period, time of transit center, and transit depth. With stellar properties now in hand, we can convert these observational results into fundamental parameters of each planet candidate. For each candidate, we fit the light curve using a physical transit model (Mandel & Agol 2002; Kipping 2010) simultaneously with the systematics model described by Foreman-Mackey et al. (2015). We use *emcee* to sample from the posterior probability distribution for the stellar—limb darkening coefficients, mass, radius, and effective temperature—and planetary—radius, period, phase, impact parameter, eccentricity, and argument of periapsis—parameters, conditioned on the light curve and the measured stellar properties. Following Foreman-Mackey et al. (2015), the likelihood function that we use is marginalized over the parameters of the systematics model. To incorporate the stellar measurements, we approximate the constraints using a three-dimensional Gaussian in mass, radius, and effective temperature.

In this analysis, we assume the dilution caused by additional stars contributing flux into the aperture is negligible for nearly all systems. Given the location of the Campaign 1 field at a high galactic latitude, we expect low contamination by background giants. Nevertheless, this assumption may not be valid for all systems. Any contamination unaccounted for, as may happen if any of these stars are actually unresolved binaries, would cause us to underestimate the radii of any planets we detect. Therefore, high-contrast adaptive optics imaging of any systems should be obtained before any of these planets are placed on a planet mass-radius diagram.

The planet parameters measured by this analysis are listed in Table 3.

4. FALSE POSITIVE ANALYSIS

There are many scenarios which can cause an astrophysical false positive, where an eclipsing binary star masquerades as a transiting planet. The most common scenarios are if (a) it is a highly grazing eclipse, or (b) the binary system shares a photometric aperture with a significantly brighter star, resulting in a diluted eclipse

¹¹ <http://www.astro.princeton.edu/~tdm/k2/>

¹² <http://phoenix.ens-lyon.fr/Grids/BT-Settl/CIFIST2011/>

depth. When possible, such astrophysical false positive scenarios are traditionally ruled out by detailed follow-up observations, often a combination of high-resolution imaging and radial-velocity measurements. However, the *Kepler* mission, with its thousands of planet candidates around mostly faint stars, necessitated a paradigm shift—a move toward probabilistic interpretation of transit signals, rather than comprehensive follow-up of each individual candidate (Morton & Johnson 2011).

Morton (2012) presented an automated method to calculate the probability that a planet candidate might be caused by an astrophysical false positive. This method uses Galactic population simulations to determine the distributions of possible false positive scenarios, comparing the typical light curve shape of each to the data. It then combines this information with observationally motivated prior assumptions about the populations of field stars, the properties of multiple star systems, and the occurrence rate of planets as determined from *Kepler* (Fressin et al. 2013), in order to determine the probability that the observed signal may be a false positive. Similar in spirit to other published methods of probabilistic validation, such as BLENDER (Torres et al. 2011) and PASTIS (Díaz et al. 2014), it has the advantage of being computationally less demanding and fully automated, and thus easily applied in batch to a large number of candidates.

In this work, we use *vespa*¹³, a new publicly available, general-purpose implementation of the Morton (2012) procedure, to calculate false positive probabilities (FPPs) for each of these *K2* candidates. The following constraints on false positive scenarios are imposed:

- A chance-aligned eclipsing binary system may reside anywhere inside or within one pixel of the photometric aperture of the target star.
- The maximum allowed depth of a potential secondary eclipse event is the most significantly detected signal at the same period of the planet candidate, once the primary transit is masked out.
- Blended stars must be allowed by the available adaptive optics and archival imaging data (discussed in detail below).

Each of these scenarios is an astrophysical eclipse, caused by one object passing in front of another, blocking some fraction of the total light. The calculations here do not include the possibility that each signal is caused by an instrumental artifact in the data or some other astrophysical event, such as stellar activity, masquerading as planet transits.

Table 4 summarizes the results of these calculations, presenting the relative probability for each candidate to be caused by any of three false positive scenarios: an undiluted eclipsing binary (EB), a hierarchical triple eclipsing binary (HEB), and a chance-aligned background(/foreground) eclipsing binary (BEB).

Four of the presented candidates have FPP >90%; these are considered to be likely false positives. On the other hand, 21 candidates have FPP < 1%. Two of these are found to be caused by systematics in the transit

search noise model (details in §5.2), and so we identify those as false positives. Four more of these 21 might plausibly be caused by contamination by detected stellar companions within the photometric apertures (see §4.2), so we keep these as candidates.

This leaves 15 candidates that we statistically validate as planets, plus three additional planets that *vespa* does not validate but have been previously identified in the literature (Crossfield et al. 2015; Armstrong et al. 2015b). So in total, of the 36 candidates, 18 are secure planets, 14 of which we here validate for the first time.

We emphasize that the majority of these validations rely solely on the transit photometry and SDSS data, with follow-up imaging only obtained for seven of the 31 targets. This demonstrates the utility of the *vespa* tool, which will be crucial to interpreting future candidates detected by *K2*, TESS, and PLATO and prioritizing follow-up observing efforts. We show the transit signals in Figure 2.

4.1. Adaptive Optics Imaging

We obtained high resolution images of seven stars with the Palomar High Angular Resolution Observer (PHARO) infrared detector (Hayward et al. 2001) behind the PALM3000 adaptive optics system (Dekany et al. 2013) at the Palomar 5.1-meter Hale telescope on the nights of 2015 February 3 and 4 UT. Sky conditions were mostly clear with light cirrus and $\approx 1''.0$ – $1''.3$ seeing on both nights. We used the smallest plate scale of 25 mas pix^{-1} which resulted in a field of view of $25''.6 \times 25''.6$ across the 1024^2 pix^2 array. All observations were obtained with the 32x pupil sampling mode, resulting in Strehl ratios of ≈ 20 – 30% in K_S for our $V=11$ – 13 mag targets as measured by the Strehl monitor at the telescope in real time. We obtained unsaturated dithered frames of each target in K_S -band with typical integration times of 2–10 s. Except for EPIC 201828749 and EPIC 201546283, which had nearby candidate binary companions, we also acquired deep saturated images (5–10 frames at 60 sec each) to search for fainter companions.

Images were registered and contrast curves were generated following Bowler et al. (2015). For the saturated data, the star’s position in each image was found by masking the saturated region and fitting a 2D bivariate Gaussian to the PSF wings. Contrast curves for the median-combined image are calibrated using the unsaturated frames. The typical sensitivity is 6.5–7.5 mag at $1''$. The images were astrometrically calibrated using dithered observations of the Trapezium cluster centered on θ^1 Ori C taken on 2015 Feb 3 UT. Based on the reference astrometry for pairs of stars in the field from McCaughrean & Stauffer (1994), we measure a plate scale of 25.2 ± 0.4 mas pix^{-1} and north orientation of $-0.2 \pm 0.3^\circ$. Since this latter value is consistent with being aligned with the detector columns, we adopt a value of $0.0 \pm 0.3^\circ$ for this work. Relative photometry of nearby stars is carried out using aperture photometry with an aperture radius of 12 pix ($0''.3$). For EPIC 201828749, we also acquired J - and H -band images. Astrometry and photometry is derived separately for each image, and the mean and standard deviation of these measurements is adopted for our final values listed in Table 5.

Images for all systems AO data was obtained for is

¹³ <http://github.com/timothymorton/vespa>

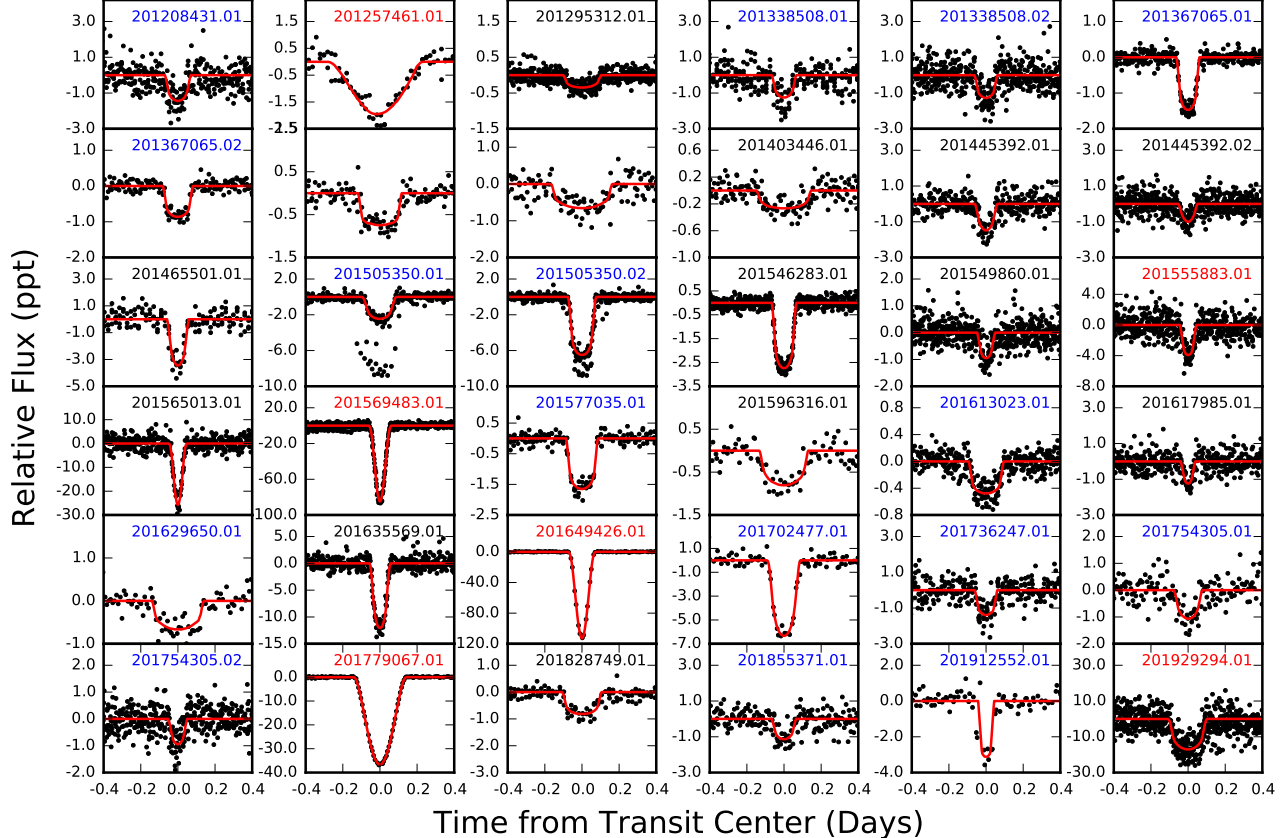


FIG. 2.— Phase-folded *K2* photometry for all planet candidates analyzed in this paper. Each is the product of a fiducial noise model, in which the median systematic has been removed for illustrative purposes. The systems which we validate as transiting planets are labeled in blue. The systems which we confirm as false positive events are labeled in red. The systems which we leave as candidates are labeled in black. Red curves outline the median transit model for each candidate system.

shown in Figure 3, while contrast curves showing the 5σ limits for detection as a function of orbital separation are given in Figure 4.

4.2. Known Background Stars

The PHARO AO system has a field of view of 25 arcseconds. Each *K2* pixel is a square, $3''.98$ on a side. A background eclipsing binary within a few *K2* pixels of our target stars could mimic a transit signal inside our aperture while evading detection by PHARO. Such wide eclipsing binaries should appear in seeing-limited ground-based surveys.

To investigate the possibility that such wide companions exist, we query the ninth data release of the Sloan Digital Sky Survey (SDSS DR9, Ahn et al. 2012). For each target, from the depth of the observed transit we determine how bright a background object must be to cause the event if the background object were an equal mass totally-eclipsing binary. We then search for all stars within $25''$ that are within this brightness limit relative to the candidate host star. All apertures we use in our *K2* analysis are smaller than $20''$ so this search should encompass the region where possible background contaminants could reside. Of the 31 stars in our sample, eleven have such a companion, plus one detected in AO imaging.

Unlike the original *Kepler* field, the field for *K2* Cam-

paign 1 is well out of the galactic plane, so the rate of giant, distant background stars is significantly lower. We include all potential contaminants in Table 5. We validate or eliminate each of these as a possibility based on the transit shape. For example, the events near EPIC 201546283 could only be caused by a background binary if the background object was a completely-eclipsing system (so that the eclipse depth was 50%). In this case, the transit would be perfectly V-shaped. Since it is not, we can rule out the possibility this background object causes the transit event.

In Table 5, the “maximum depth” column represents the maximum observed “transit” depth if the transit were actually caused by a total eclipse of the hypothetical background binary system, inducing a 50% flux decrement in the background star’s apparent brightness.

The photometric apertures used to detect these candidates range in radius from $10''.0$ to $19''.9$. In order to be a plausible contaminant, any companion star must be either within this aperture or just outside but bright enough for significant flux to leak in. Evaluating each of the systems listed in Table 5, we judge that we cannot yet rule out contamination as a potential source of the transit signal for four candidates: 201295312.01, 201403446.01, 201546283.01, and 201828749.01. Despite receiving low FPP scores from *vespa*, we list these systems as candidates in Table 4, rather than planets. Further updates to

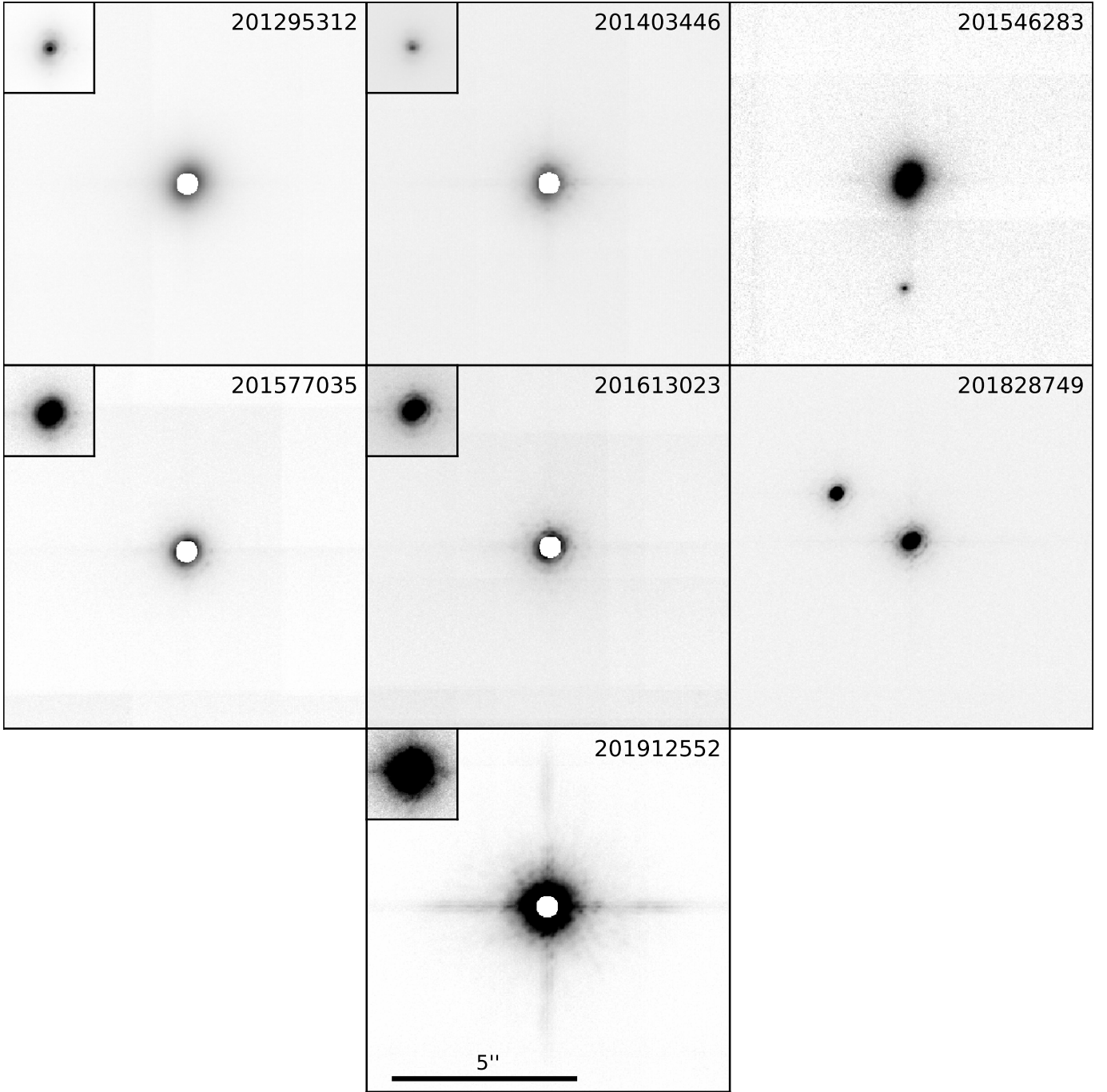


FIG. 3.— Adaptive optics images for the seven stars observed with high-contrast imaging. The main frame for each single system shows the deep, saturated image. The inset for each single system shows a shallower, unsaturated image to better identify companions at close projected orbital separations. For the two systems with imaged companions, EPIC 201546283 and EPIC 201828749, only unsaturated frames are collected. The pixel scale is $0''.0252$ per pixel. Each subplot is a square 400 pixels on a side and each inset is a square 100 pixels on a side. All subplots, including insets, are plotted on the same scale.

the *vespa* code will allow consideration of “specific” false positive scenarios; that is, scenarios that correspond to actually detected stars such as these, rather than hypothetical background or bound companions.

The candidates with identified companions that we judge to not be plausible sources of potential contamination are the following:

- 201546283.01— For this system, the “maximum depth” is nearly identical to the observed transit depth, which would require a perfectly V-shaped

eclipse to explain. As this is not the case (see Figure 2), this signal cannot be caused by contamination from this star.

- 201629650.01— The companion to this star is $17''.3$ from the EPIC target. As this is outside the aperture (radius $15''.9$) and the background star is not particularly bright, we rule out contamination for this system.
- 201702477.01— The companion to this star is

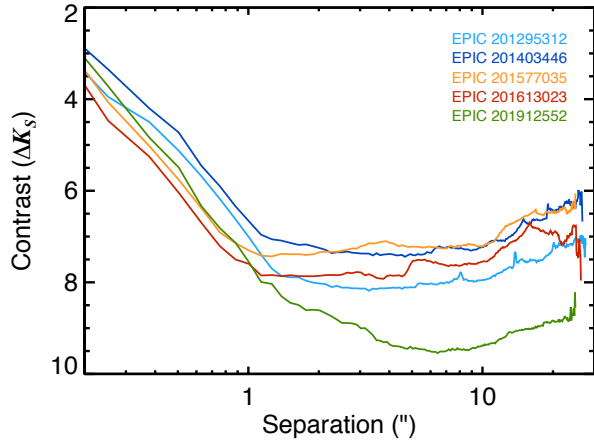


FIG. 4.— 5σ contrast curves for all systems with AO nondetections. For all systems, we can exclude the possibility that a companion at a given ΔK_S exists. From our known transit depths, we can then rule out significant parameter space in which an eclipsing binary could reside and mimic a transit signal.

$12''.15$ from the EPIC target, and the aperture size is $10''.0$. In addition, the maximum depth in this system is almost identical to the transit depth. For these two reasons we rule out contamination in this case.

SDSS is 95% complete at $r = 22.2$ mag and the telescope has a point spread function of $1''.4$. For the purposes of the *vespa* calculation, we thus treat nondetection in SDSS data as providing a contrast curve at wide separations down to a limiting magnitude of $r = 22.2$ mag.

4.3. Archival Imaging

For the stars with AO nondetections, there is still the possibility that a background binary could be positioned directly behind the target star, evading detection. The probability is small, given the $0''.1$ diffraction limit of the Hale Telescope at $2\ \mu\text{m}$, but nonzero. While the *vespa* calculations quantify this probability for this to occur, we can also rule out the possibility of such chance alignments, down to a certain contrast, with archival imaging data.

We include this extra analysis step for EPIC 201912552, considering the additional follow-up this target may warrant. We download data from the POSS I and II surveys, which imaged EPIC 201912552 in 1955 and 1989, respectively. This star has a proper motion of $-74 \pm 2\ \text{mas yr}^{-1}$ in right ascension and $-122 \pm 4\ \text{mas yr}^{-1}$ in declination, so it has moved by $8''.35$ since the POSS I data were collected. As shown in Figure 5, we do not detect any targets at the present-day location of EPIC 201912552 in either of the POSS surveys.

For this target, we can extend our contrast curves to zero present-day orbital separation and rule out the possibility that these transit events are caused by a background eclipsing binary. By combining present-day seeing-limited photometric survey data, adaptive optics imaging, and archival photometry, the only stellar companions we would not detect would be those that are gravitationally bound to the target star and positioned in their orbits so that their projected separation is smaller

than the diffraction limit of the Hale Telescope. Such an alignment would require the orbital inclination of the binary to be nearly 90° and the phase $\varpi + \theta \approx \pi/2$ or $3\pi/2$. While we cannot fully rule out this possibility, the *vespa* calculations confirm that its probability is negligibly small.

4.4. TRES Radial Velocities

We observed EPIC 201912552 on 2015 February 04 and 25 UT with the Tillinghast Reflector Echelle Spectrograph (TRES) on the 1.5 m Tillinghast Reflector at the Fred L. Whipple Observatory. These dates were chosen to be near the times of largest RV variations, corresponding to phases of 0.72 and 0.32 relative to the time of transit. The spectra were taken with a resolving power of $R = 44,000$ and integration times ranging from 2800 to 3600 seconds, resulting in signal-to-noise ratios between 17 and 29 per resolution element.

The spectra were extracted as described in Buchhave et al. (2010). The relative RVs were derived by cross-correlating the spectra against the strongest observed spectrum (in this case, the first) over the wavelength range 4700 - 6800 Angstroms. We selected 19 echelle orders in the analysis, being careful to reject orders with telluric absorption lines, fringing in the far red and those with very low SNR in the blue.

The two observed spectra have RVs that differ by $47 \pm 42\ \text{m s}^{-1}$. If the RVs were caused by a stellar companion, the RV shift between these observations would be on the order of km s^{-1} . Therefore, we can rule out any stellar-mass companions that would be able to create this transit signal.

5. POTENTIALLY INTERESTING SYSTEMS

5.1. A Mini-Neptune with Earthlike Insolation

The planet orbiting EPIC 201912552 may be an interesting target for atmospheric studies of transiting exoplanets.

By combining archival and modern seeing-limited data with adaptive optics imaging, we can exclude the possibility these transit events are caused by a background eclipsing binary. The apparent transits must be caused by an object co-moving with EPIC 201912552; radial velocities eliminate the possibility the companion is non-planetary. Therefore, we confirm the planetary nature of this system.

This star is an M2.8 dwarf at a distance of 34 ± 4 pc. Of our planet candidate hosts, only EPIC 201367065 (originally discovered by Crossfield et al. 2015) is brighter in K -band. This star is only 0.1 magnitudes fainter in K than GJ 1214 (Charbonneau et al. 2009). Due to the relative brightness of the host star, this target is likely to become a prime target for atmospheric characterization studies and is ideal as a target for future space-based missions such as *JWST*.

The planet is slightly smaller than GJ 1214b, but unlike that planet, EPIC 201912552b is not highly irradiated. Instead, it is at a reduced semimajor axis $a/R_\star = 84.3 \pm 9.5$. Its equilibrium temperature is then, assuming zero albedo, $T_{eq} = 271 \pm 16\ \text{K}$, meaning its bulk insolation is 128 ± 28 percent that of the Earth's. Although the planet is likely too large to be rocky (Rogers 2014), its atmosphere is likely to be the focus of many fu-

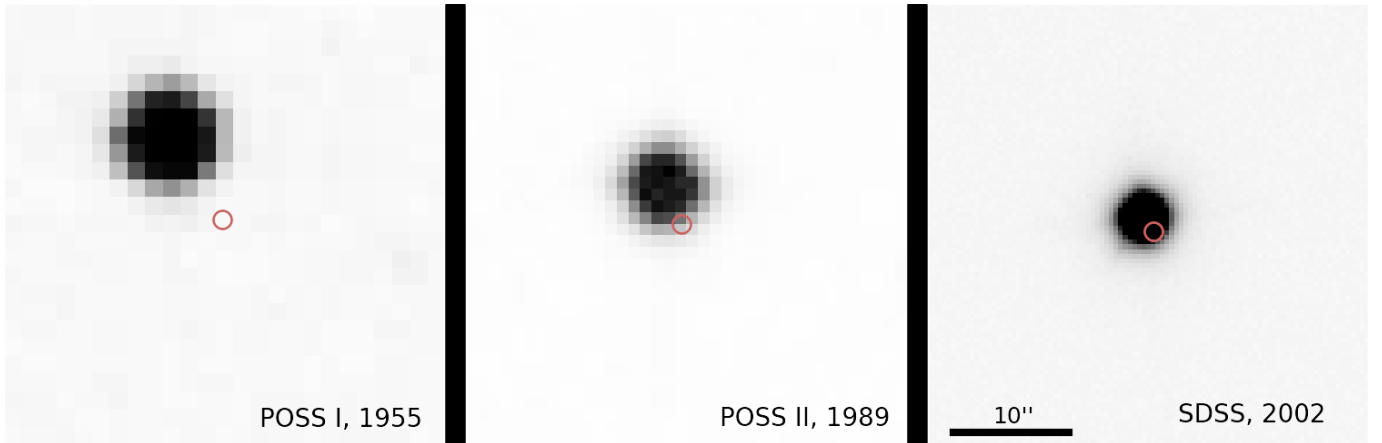


FIG. 5.— Imaging for EPIC 201912552 from 1955 to 2002. There is no background object directly behind the present day location of the target (red circle) that could be missed by the AO observations, while modern SDSS imaging can rule out wide companions that may have been missed at wide separations, beyond the AO field of view. All subplots are on the same scale.

ture observations, providing a cool analogue to the highly irradiated planets of a similar size found by *Kepler*.

5.2. Non-Astrophysical False Positives

The method of Foreman-Mackey et al. (2015) assumes that all variability in the light curves are caused by either the motion of *K2*, in which case the variability is shared by all stars, or transits of planets, in which case the variability is intrinsic to only one star. This assumption breaks down for extremely spotted stars where the astrophysical variability is larger than the instrumental magnitude. In that regime, the starspot modulations can be incorrectly fit by the systematic model, causing spurious transits to appear. This appears to be the case with EPIC 201929294, which has coherent starspots that appear to have the same rotation period as the transit period reported previously. Because the starspots are so periodic and coherent, these spurious transits were falsely identified as a planet candidate; we consider that system a false positive in this work.

The planet candidate possibly orbiting EPIC 201555883 has a period, time of transit, and transit duration consistent with EPIC 201569483. Such effects are not uncommon in *Kepler* data. Coughlin et al. (2014) identify 685 KOIs as false positives and outline four physical reasons why these anomalies may occur. EPIC 201555883 is a unique case in that it does not appear to fall under any of these cases. It falls on module 23, while EPIC 201569483 is on module 8, neither 180 degrees away from nor on the same column as this candidate. Moreover, there is not any evidence of a mechanism that could cause a third star to induce both the appearance of a 7% eclipse on one module and an additional anomalous transit event on a different module. Instead, this candidate could be a false positive caused by a different systematic mechanism.

Foreman-Mackey et al. (2015) modeled the systematic effects in the *K2* light curves using a linear combination of “eigen light curves” generated empirically by running a principle component analysis on the light curves of every star. This means that the training set includes the light curves for variable stars, eclipsing binaries, and even transiting planets. Again, this star has significant variability caused by starspots. In this case, the fitting procedure tries to account for stellar variability using

the eigen light curves. This overfit gives undue weight to eigen light curves that include the transits of EPIC 201569483, causing this spurious transit to occur. Again, we consider this system to be a false positive.

The problem of over-fitting stellar variability using eigen light curves can be solved by adding a stellar activity model to our fitting procedure. In this case, the spacecraft motion could be fit simultaneously with a model of starspot modulation, astroseismic oscillations, and planet transits. Such a model is currently under development (Angus et al. *in prep*).

5.3. Multiple Planet Systems

Five of the systems reported by Foreman-Mackey et al. (2015) have more than one transiting candidate. One of these is EPIC 201367065, a three-planet system originally announced by Crossfield et al. (2015). Another of these is EPIC 201505350 (Armstrong et al. 2015b), a two-planet system with the orbital periods of the two planets near a 3:2 period commensurability. The remaining three are all representative of the multiple-planet systems observed by *Kepler* (Lissauer et al. 2011; Fabrycky et al. 2014). Two of the systems are near a period commensurability and all three consist of mini-Neptune sized planets.

We do not detect any significant transit timing variations (TTVs) in any of these systems from the *K2* data alone. EPIC 201338508 would be expected to have a TTV period of 117 days, but is likely too far from commensurability to have an observable TTV signal. EPIC 201445392 is expected to have a TTV period of 234 days, so this system may be a candidate for additional follow-up to constrain the system masses dynamically. The transiting planets orbiting EPIC 201754305 are near a 5:2 period commensurability. There is no evidence from *Kepler* of an abundance of planets near this period ratio, and so this may be coincidence. Follow-up observations may be warranted to search for an additional planet in this system forming a resonant chain, similar to those observed around other stars (e.g. Swift et al. 2013; Campante et al. 2015).

5.4. Systems Orbiting Bright Stars

One of the primary goals of *K2* is the detection of transiting planets around bright stars that can be followed up

from the ground or with future space-based observatories such as JWST (Howell et al. 2014). Of our sample, two systems orbit stars with $K < 9$ mag: EPIC 201367065 (Crossfield et al. 2015) and EPIC 201912552. An additional planet candidate may orbit EPIC 201828749, a star with $K = 9.93 \pm 0.03$ mag. These targets are ideal for ground-based followup and may be useful targets for Spitzer and JWST to probe planetary atmospheres.

6. RESULTS AND DISCUSSION

We have presented stellar parameters for all planet candidates systems identified by Foreman-Mackey et al. (2015). We statistically validate 18 of the 36 candidates as bona fide planets, and we identify 6 as false positives. Of these planets, 4 have been previously validated in other works, while 14 are validated here for the first time. The systems not validated as planets or false positives remain as planet candidates.

Enabling much of this analysis are two new open-source Python packages: *isochrones*¹⁴, which we use to infer posteriors on physical stellar properties based on fitting theoretical stellar models to observed data; and *vespa*¹⁵, a new implementation of the Morton (2012) transit false positive analysis scheme. Both of these packages will continue to be useful in future analysis of transit candidates where comprehensive follow-up observations may be unavailable.

With the exception of one object, all of the stellar parameters are derived from comparing photometric observations to the Dartmouth stellar evolution models. As a result, both the stellar and planet parameters are subject to systematic biases induced by discrepancies between the models and reality.

As stated in §2.2, we infer stellar parameters using the Dartmouth models, with a mass upper limit of $3.7M_{\odot}$. Given the location of the Campaign 1 field with respect to the galactic plane, we expect a low contamination rate by halo giants. However, there are a few stars that are possibly miscategorized giants. EPIC 201257461 is identified in the RAdial Velocity Experiment (RAVE) Fourth Data Release as a target with $\log(g) = 3.18$, consistent with that of a giant star. It is therefore perhaps not surprising that this system is flagged as a false positive based on the transit shape. EPIC 201929294, with a proper motion of $0.010'' \text{ yr}^{-1}$ (Zacharias et al. 2012) has a reduced proper motion consistent with that of a giant star. While suggestive, this observation does not definitively provide information about the nature of this target. Likewise, our false positive analysis is neither able to confirm nor exclude the planetary nature of the observed transit signal around this target.

The planets we confirm in this paper, like the planets found in the original *Kepler* mission, span a wide range of parameter space. They are at distances ranging from 34 to 700 pc, have radii ranging from 1.3 to $5.3 R_{\oplus}$, and orbit with periods ranging from 5.0 to 50.3 days. Like the original mission, we find significantly more small planets than large planets, as expected from the radius distributions measured from *Kepler* (Howard et al. 2012; Fressin et al. 2013; Morton & Swift 2014).

Unlike the original mission, however, we find that

nearly all of our confirmed planets are around stars less massive than the Sun. This difference is a result of both the Campaign 1 field and the target selection process. Campaign 1 is at a significantly higher galactic latitude than the original *Kepler* mission, meaning there is a much lower number density of targets at large distances. As massive stars at kiloparsec distances are relatively less likely to exist in Campaign 1 than near the galactic plane, the pool of targets that could be selected for Campaign 1 contains a larger fraction of subsolar stars.

Low-mass stars, particularly M dwarfs, are also a specific focus of the *K2* mission. One of the primary goals of the *Kepler* mission was to “determine the abundance of terrestrial and larger planets in or near the habitable zone of a wide variety of spectral types of stars” (Batalha et al. 2013). However, $\sim 70\%$ of *Kepler*’s target stars had masses within 20% of the Sun’s, while 70% of the stars in the Galaxy have less than 50% the mass of the Sun (Brown et al. 2011). *K2* will fulfill the promise of *Kepler*, with the goal of providing a yield of small planets around bright, small stars to facilitate follow-up measurements (Howell et al. 2014). This is clear from the *K2* target selection process, with thousands of K and M dwarfs being selected in each campaign. Based on these plans, we expect that *K2* will detect hundreds of planets during its lifetime, with the majority being mini-Neptunes and super-Earths around stars less massive than the Sun.

We thank Roberto Sanchis-Ojeda (Berkeley), Dan Huber (Sydney) and Jeff Coughlin (SETI) for conversations and suggestions which improved the quality of this manuscript.

We are grateful to the entire *Kepler* team, past and present. Their tireless efforts were all essential to the tremendous success of the mission and the successes of *K2* present and future.

Some of the data presented in this paper were obtained from the Mikulski Archive for Space Telescopes (MAST). STScI is operated by the Association of Universities for Research in Astronomy, Inc., under NASA contract NAS5-26555. For MAST for non-HST data is provided by the NASA Office of Space Science via grant NNX13AC07G and by other grants and contracts.

This paper includes data collected by the *Kepler* mission. Funding for the *Kepler* mission is provided by the NASA Science Mission directorate.

This paper includes data collected by the Sloan Digital Sky Survey. Funding for SDSS-III has been provided by the Alfred P. Sloan Foundation, the Participating Institutions, the National Science Foundation, and the U.S. Department of Energy Office of Science. The SDSS-III web site is <http://www.sdss3.org/>. SDSS-III is managed by the Astrophysical Research Consortium for the Participating Institutions of the SDSS-III Collaboration including the University of Arizona, the Brazilian Participation Group, Brookhaven National Laboratory, Carnegie Mellon University, University of Florida, the French Participation Group, the German Participation Group, Harvard University, the Instituto de Astrofísica de Canarias, the Michigan State/Notre Dame/JINA Participation Group, Johns Hopkins University, Lawrence Berkeley National Laboratory, Max Planck Institute for Astrophysics, Max Planck Institute for Extraterrestrial Physics, New Mex-

¹⁴ <http://github.com/timothymorton/isochrones>

¹⁵ <http://github.com/timothymorton/vespa>

ico State University, New York University, Ohio State University, Pennsylvania State University, University of Portsmouth, Princeton University, the Spanish Participation Group, University of Tokyo, University of Utah, Vanderbilt University, University of Virginia, University of Washington, and Yale University.

B.T.M. is supported by the National Science Foundation Graduate Research Fellowship under Grant No. DGE-1144469. J.A.J. is supported by generous grants from the David and Lucile Packard Foundation and the

Alfred P. Sloan Foundation.

D.F.M. and D.W.H. were partially supported by the National Science Foundation (grant IIS-1124794), the National Aeronautics and Space Administration (grant NNX12AI50G), and the Moore-Sloan Data Science Environment at NYU.

T.D.M. is supported by the National Aeronautics and Space Administration (grant NNX14AE11G).

Facilities: Kepler, PO:Hale (PHARO), FLWO:1.5m, IRTF:SpeX

REFERENCES

- Ahn, C. P., Alexandroff, R., Allende Prieto, C., et al. 2012, *ApJS*, 203, 21
- Aigrain, S., Hodgkin, S. T., Irwin, M. J., Lewis, J. R., & Roberts, S. J. 2015, *MNRAS*, 447, 2880
- Aldering, G., Adam, G., Antilogus, P., et al. 2002, in *Proc. SPIE*, ed. J. A. Tyson & S. Wolff, Vol. 4836, 61–72
- Aldering, G., Antilogus, P., Bailey, S., et al. 2006, *ApJ*, 650, 510
- Allard, F., Homeier, D., Freytag, B., et al. 2013, *Memorie della Societa Astronomica Italiana Supplementi*, 24, 128
- Armstrong, D. J., Kirk, J., Lam, K. W. F., et al. 2015a, *ArXiv e-prints*, arXiv:1502.04004
- Armstrong, D. J., Veras, D., Barros, S. C. C., et al. 2015b, *ArXiv e-prints*, arXiv:1503.00692
- Bacon, R., Copin, Y., Monnet, G., et al. 2001, *MNRAS*, 326, 23
- Barentsen, G. 2015, *K2fix: Kepler pixel data visualizer*, *Astrophysics Source Code Library*, ascl:1503.001
- Batalha, N. M., Rowe, J. F., Bryson, S. T., et al. 2013, *ApJS*, 204, 24
- Boisse, I., Bouchy, F., Hébrard, G., et al. 2011, *A&A*, 528, A4
- Borucki, W. J., Koch, D., Basri, G., et al. 2010, *Science*, 327, 977
- Borucki, W. J., Koch, D. G., Basri, G., et al. 2011a, *ApJ*, 728, 117
- , 2011b, *ApJ*, 736, 19
- Bowler, B. P., Liu, M. C., Shkolnik, E. L., & Tamura, M. 2015, *ApJS*, 216, 7
- Boyajian, T. S., von Braun, K., van Belle, G., et al. 2012, *ApJ*, 757, 112
- Brown, T. M., Latham, D. W., Everett, M. E., & Esquerdo, G. A. 2011, *AJ*, 142, 112
- Buchhave, L. A., Bakos, G. Á., Hartman, J. D., et al. 2010, *ApJ*, 720, 1118
- Burke, C. J., Bryson, S. T., Mullally, F., et al. 2014, *ApJS*, 210, 19
- Campante, T. L., Barclay, T., Swift, J. J., et al. 2015, *ApJ*, 799, 170
- Charbonneau, D., Berta, Z. K., Irwin, J., et al. 2009, *Nature*, 462, 891
- Coughlin, J. L., Thompson, S. E., Bryson, S. T., et al. 2014, *AJ*, 147, 119
- Crossfield, I. J. M., Petigura, E., Schlieder, J., et al. 2015, *ArXiv e-prints*, arXiv:1501.03798
- Cushing, M. C., Vacca, W. D., & Rayner, J. T. 2004, *PASP*, 116, 362
- Cutri, R. M., & et al. 2013, *VizieR Online Data Catalog*, 2328, 0
- Cutri, R. M., Skrutskie, M. F., van Dyk, S., et al. 2003, *2MASS All Sky Catalog of point sources*.
- Dekany, R., Roberts, J., Burruss, R., et al. 2013, *ApJ*, 776, 130
- Désert, J.-M., Charbonneau, D., Torres, G., et al. 2015, *ArXiv e-prints*, arXiv:1503.03173
- Díaz, R. F., Almenara, J. M., Santerne, A., et al. 2014, *MNRAS*, 441, 983
- Dotter, A., Chaboyer, B., Jevremović, D., et al. 2008, *ApJS*, 178, 89
- Fabrycky, D. C., Lissauer, J. J., Ragozzine, D., et al. 2014, *ApJ*, 790, 146
- Ferreira, P. G., & Jaffe, A. H. 2000, *MNRAS*, 312, 89
- Foreman-Mackey, D., Hogg, D. W., Lang, D., & Goodman, J. 2013, *PASP*, 125, 306
- Foreman-Mackey, D., Montet, B. T., Hogg, D. W., et al. 2015, *ArXiv e-prints*, arXiv:1502.04715
- Fressin, F., Torres, G., Charbonneau, D., et al. 2013, *ArXiv e-prints*, arXiv:1301.0842
- Gaidos, E., Mann, A. W., Lépine, S., et al. 2014, *MNRAS*, 443, 2561
- Goodman, J., & Weare, J. 2010, *Communications in Applied Mathematics and Computational Science*, 5, 65
- Grunblatt, S. K., Howard, A. W., & Haywood, R. D. 2015, *ArXiv e-prints*, arXiv:1501.00369
- Hayden, M. R., Bovy, J., Holtzman, J. A., et al. 2015, *ArXiv e-prints*, arXiv:1503.02110
- Hayward, T. L., Brandl, B., Pirger, B., et al. 2001, *PASP*, 113, 105
- Haywood, R. D., Collier Cameron, A., Queloz, D., et al. 2014, *MNRAS*, 443, 2517
- Henden, A., & Munari, U. 2014, *Contributions of the Astronomical Observatory Skalnaté Pleso*, 43, 518
- Howard, A. W., Marcy, G. W., Bryson, S. T., et al. 2012, *ApJS*, 201, 15
- Howell, S. B., Sobeck, C., Haas, M., et al. 2014, *PASP*, 126, 398
- Huber, D., Silva Aguirre, V., Matthews, J. M., et al. 2014, *ApJS*, 211, 2
- Kipping, D. M. 2010, *MNRAS*, 408, 1758
- Lantz, B., Aldering, G., Antilogus, P., et al. 2004, in *Society of Photo-Optical Instrumentation Engineers (SPIE) Conference Series*, Vol. 5249, *Society of Photo-Optical Instrumentation Engineers (SPIE) Conference Series*, ed. L. Mazuray, P. J. Rogers, & R. Wartmann, 146–155
- Lissauer, J. J., Ragozzine, D., Fabrycky, D. C., et al. 2011, *ApJS*, 197, 8
- Lissauer, J. J., Marcy, G. W., Rowe, J. F., et al. 2012, *ApJ*, 750, 112
- Mandel, K., & Agol, E. 2002, *ApJ*, 580, L171
- Mann, A. W., Brewer, J. M., Gaidos, E., Lépine, S., & Hilton, E. J. 2013a, *AJ*, 145, 52
- Mann, A. W., Feiden, G. A., Gaidos, E., & Boyajian, T. 2015, *ArXiv e-prints*, arXiv:1501.01635
- Mann, A. W., Gaidos, E., & Ansdell, M. 2013b, *ApJ*, 779, 188
- McCaughrean, M. J., & Stauffer, J. R. 1994, *AJ*, 108, 1382
- Montet, B. T., Johnson, J. A., Muirhead, P. S., et al. 2015, *ApJ*, 800, 134
- Morton, T. D. 2012, *ApJ*, 761, 6
- Morton, T. D., & Johnson, J. A. 2011, *ApJ*, 738, 170
- Morton, T. D., & Swift, J. 2014, *ApJ*, 791, 10
- Mullally, F., Coughlin, J. L., Thompson, S. E., et al. 2015, *ArXiv e-prints*, arXiv:1502.02038
- Newton, E. R., Charbonneau, D., Irwin, J., & Mann, A. W. 2015, *ApJ*, 800, 85
- Ochsenbein, F., Bauer, P., & Marcout, J. 2000, *A&AS*, 143, 23
- Rayner, J. T., Toomey, D. W., Onaka, P. M., et al. 2003, *PASP*, 115, 362
- Rogers, L. A. 2014, *ArXiv e-prints*, arXiv:1407.4457
- Rowe, J. F., Bryson, S. T., Marcy, G. W., et al. 2014, *ApJ*, 784, 45
- Rowe, J. F., Coughlin, J. L., Antoci, V., et al. 2015, *ArXiv e-prints*, arXiv:1501.07286
- Swift, J. J., Johnson, J. A., Morton, T. D., et al. 2013, *ApJ*, 764, 105
- Thompson, B., Frinchaboy, P., Kinemuchi, K., Sarajedini, A., & Cohen, R. 2014, *AJ*, 148, 85
- Torres, G., Fressin, F., Batalha, N. M., et al. 2011, *ApJ*, 727, 24
- Vacca, W. D., Cushing, M. C., & Rayner, J. T. 2003, *PASP*, 115, 389
- Vanderburg, A., & Johnson, J. A. 2014, *PASP*, 126, 948

- Vanderburg, A., Montet, B. T., Johnson, J. A., et al. 2015, *ApJ*, 800, 59
- Zacharias, N., Finch, C. T., Girard, T. M., et al. 2012, *VizieR Online Data Catalog*, 1322, 0

TABLE 1
PHOTOMETRY FOR ALL OBJECTS OF INTEREST

EPIC	B_{APASS}	V_{APASS}	g_{APASS}	r_{APASS}	i_{APASS}	J_{2MASS}	H_{2MASS}	K_{2MASS}	W1	W2	W3
201208431	16.23 ± 0.05	14.91 ± 0.03	15.56 ± 0.04	14.29 ± 0.07	13.89 ± 0.12	12.37 ± 0.02	11.75 ± 0.02	11.57 ± 0.02	11.51 ± 0.02	11.55 ± 0.02	11.58 ± 0.20
201257461	12.82 ± 0.03	11.77 ± 0.01	12.24 ± 0.04	11.49 ± 0.01	11.19 ± 0.02	9.99 ± 0.02	9.48 ± 0.02	9.37 ± 0.02	9.28 ± 0.02	9.37 ± 0.02	9.30 ± 0.04
201295312	12.78 ± 0.04	12.19 ± 0.12	12.41 ± 0.03	12.08 ± 0.09	12.01 ± 0.21	11.02 ± 0.03	10.70 ± 0.02	10.69 ± 0.02	10.63 ± 0.02	10.69 ± 0.02	10.75 ± 0.12
201338508	16.30 ± 0.07	14.91 ± 0.03	15.62 ± 0.05	14.33 ± 0.02	13.79 ± 0.05	12.45 ± 0.03	11.76 ± 0.02	11.60 ± 0.02	11.49 ± 0.03	11.49 ± 0.02	11.16 ± 0.13
201367065	13.52 ± 0.06	12.17 ± 0.01	12.87 ± 0.03	11.58 ± 0.02	10.98 ± 0.17	9.42 ± 0.03	8.80 ± 0.04	8.56 ± 0.02	8.44 ± 0.02	8.42 ± 0.02	8.32 ± 0.02
201384232	13.30 ± 0.05	12.65 ± 0.04	12.91 ± 0.05	12.48 ± 0.06	12.34 ± 0.07	11.44 ± 0.02	11.09 ± 0.02	11.07 ± 0.02	11.00 ± 0.02	11.05 ± 0.02	11.21 ± 0.16
201393098	13.90 ± 0.04	13.21 ± 0.03	13.54 ± 0.06	13.02 ± 0.04	12.85 ± 0.05	11.95 ± 0.02	11.63 ± 0.02	11.56 ± 0.02	11.52 ± 0.02	11.57 ± 0.02	11.61 ± 0.21
201403446	12.48 ± 0.02	12.03 ± 0.02	12.18 ± 0.01	11.94 ± 0.05	11.86 ± 0.04	11.05 ± 0.03	10.76 ± 0.02	10.78 ± 0.02	10.67 ± 0.03	10.71 ± 0.02	10.36 ± 0.07
201445392	15.73 ± 0.02	14.61 ± 0.03	15.19 ± 0.04	14.29 ± 0.02	14.03 ± 0.07	12.83 ± 0.03	12.32 ± 0.03	12.24 ± 0.03	12.16 ± 0.02	12.21 ± 0.02	—
201465501	—	—	16.73 ± 0.02	15.18 ± 0.03	14.35 ± 0.15	12.45 ± 0.02	11.71 ± 0.02	11.49 ± 0.02	11.35 ± 0.02	11.21 ± 0.02	11.35 ± 0.19
201505350	13.80 ± 0.02	13.00 ± 0.01	13.36 ± 0.02	12.76 ± 0.01	12.57 ± 0.02	11.60 ± 0.02	11.21 ± 0.02	11.16 ± 0.03	11.10 ± 0.02	11.13 ± 0.02	10.95 ± 0.12
201546283	13.51 ± 0.07	12.64 ± 0.02	13.03 ± 0.02	12.37 ± 0.02	12.17 ± 0.05	11.16 ± 0.02	10.79 ± 0.03	10.70 ± 0.02	10.61 ± 0.02	10.66 ± 0.02	10.53 ± 0.09
201549860	15.56 ± 0.06	14.37 ± 0.05	14.95 ± 0.07	13.85 ± 0.03	13.45 ± 0.05	12.14 ± 0.02	11.56 ± 0.02	11.42 ± 0.02	11.38 ± 0.02	11.46 ± 0.02	11.60 ± 0.25
201555883	16.48 ± 0.01	15.43 ± 0.01	16.19 ± 0.10	15.09 ± 0.13	14.55 ± 0.08	13.20 ± 0.02	12.53 ± 0.03	12.43 ± 0.03	12.34 ± 0.02	12.38 ± 0.03	—
201565013	—	—	18.25 ± 0.01	16.91 ± 0.01	16.34 ± 0.01	14.78 ± 0.04	14.11 ± 0.05	14.08 ± 0.07	13.94 ± 0.03	13.87 ± 0.04	—
201569483	12.90 ± 0.08	12.05 ± 0.07	12.44 ± 0.03	11.76 ± 0.08	11.48 ± 0.08	10.39 ± 0.02	9.97 ± 0.03	9.88 ± 0.02	9.82 ± 0.02	9.87 ± 0.02	9.82 ± 0.05
201577035	13.14 ± 0.11	12.42 ± 0.02	12.70 ± 0.04	12.21 ± 0.03	12.13 ± 0.20	11.06 ± 0.02	10.75 ± 0.02	10.64 ± 0.02	10.64 ± 0.02	10.69 ± 0.02	10.55 ± 0.10
201596316	14.21 ± 0.01	13.39 ± 0.09	13.78 ± 0.07	13.14 ± 0.12	12.88 ± 0.10	11.87 ± 0.02	11.46 ± 0.02	11.35 ± 0.02	11.29 ± 0.02	11.35 ± 0.02	10.80 ± 0.11
201613023	12.99 ± 0.09	12.26 ± 0.01	12.56 ± 0.03	12.05 ± 0.03	11.96 ± 0.08	10.98 ± 0.02	10.71 ± 0.02	10.61 ± 0.02	10.58 ± 0.02	10.63 ± 0.02	10.59 ± 0.10
201617985	16.34 ± 0.02	14.86 ± 0.05	15.62 ± 0.06	14.26 ± 0.08	13.42 ± 0.09	11.72 ± 0.02	11.09 ± 0.04	10.90 ± 0.02	10.73 ± 0.02	10.70 ± 0.02	10.86 ± 0.11
201629650	13.61 ± 0.03	12.90 ± 0.04	13.20 ± 0.03	12.73 ± 0.01	12.53 ± 0.06	11.57 ± 0.03	11.26 ± 0.02	11.17 ± 0.03	11.14 ± 0.02	11.18 ± 0.02	10.93 ± 0.12
201635569	17.74 ± 0.16	16.31 ± 0.01	17.02 ± 0.01	15.62 ± 0.01	14.87 ± 0.01	13.42 ± 0.03	12.77 ± 0.02	12.61 ± 0.03	12.52 ± 0.03	12.55 ± 0.03	—
201649426	14.57 ± 0.03	13.53 ± 0.01	14.04 ± 0.01	13.18 ± 0.02	12.86 ± 0.06	11.57 ± 0.02	11.07 ± 0.02	11.07 ± 0.02	10.88 ± 0.02	10.91 ± 0.02	10.86 ± 0.12
201702477	15.27 ± 0.05	14.57 ± 0.04	14.89 ± 0.04	14.40 ± 0.06	14.24 ± 0.03	13.27 ± 0.03	12.88 ± 0.03	12.77 ± 0.03	12.81 ± 0.02	12.84 ± 0.03	—
201736247	15.49 ± 0.06	14.66 ± 0.05	15.01 ± 0.04	14.35 ± 0.04	14.14 ± 0.02	13.07 ± 0.02	12.55 ± 0.02	12.49 ± 0.03	12.46 ± 0.02	12.50 ± 0.02	12.34 ± 0.46
201754305	15.65 ± 0.04	14.65 ± 0.01	15.13 ± 0.04	14.28 ± 0.01	13.93 ± 0.05	12.76 ± 0.03	12.21 ± 0.03	12.09 ± 0.02	12.06 ± 0.02	12.10 ± 0.02	12.34 ± 0.46
201779067	11.81 ± 0.01	11.27 ± 0.01	11.53 ± 0.07	11.12 ± 0.01	10.95 ± 0.01	10.13 ± 0.02	9.87 ± 0.02	9.80 ± 0.02	9.74 ± 0.02	9.77 ± 0.02	9.74 ± 0.04
201828749	12.48 ± 0.04	11.76 ± 0.01	12.13 ± 0.05	11.58 ± 0.04	11.32 ± 0.04	10.49 ± 0.03	10.23 ± 0.04	9.93 ± 0.03	9.82 ± 0.02	9.87 ± 0.02	9.98 ± 0.06
201855371	14.82 ± 0.06	13.52 ± 0.04	14.20 ± 0.06	12.96 ± 0.03	12.45 ± 0.01	11.08 ± 0.02	10.44 ± 0.02	10.31 ± 0.02	10.22 ± 0.02	10.26 ± 0.02	10.12 ± 0.07
201912552	15.01 ± 0.06	13.50 ± 0.05	14.22 ± 0.05	12.86 ± 0.04	11.66 ± 0.08	9.76 ± 0.03	9.13 ± 0.03	8.90 ± 0.02	8.77 ± 0.02	8.67 ± 0.02	8.55 ± 0.03
201929294	14.32 ± 0.04	13.31 ± 0.03	13.78 ± 0.05	12.97 ± 0.07	12.61 ± 0.09	11.48 ± 0.03	10.98 ± 0.02	10.80 ± 0.02	10.73 ± 0.02	10.78 ± 0.02	10.67 ± 0.10

TABLE 2
STELLAR PROPERTIES FOR ALL OBJECTS OF INTEREST

EPIC	RA (J2000) (Hours)	Dec (J2000) (Degrees)	Mass (M_{\odot})	Radius (R_{\odot})	T_{eff} (K)	[Fe/H] (dex)	Distance (pc)
201208431	11.6497093	-3.905585	$0.64^{+0.04}_{-0.04}$	$0.61^{+0.03}_{-0.04}$	4180^{+41}_{-45}	$-0.05^{+0.18}_{-0.18}$	222^{+13}_{-17}
201257461	11.8774073	-3.094936	$0.66^{+0.06}_{-0.04}$	$0.63^{+0.06}_{-0.04}$	4809^{+46}_{-37}	$-0.47^{+0.22}_{-0.28}$	91^{+10}_{-6}
201295312	11.6007753	-2.520881	$1.05^{+0.06}_{-0.08}$	$1.01^{+0.10}_{-0.07}$	5942^{+80}_{-73}	$-0.02^{+0.17}_{-0.20}$	307^{+31}_{-24}
201338508	11.2869001	-1.877976	$0.58^{+0.07}_{-0.06}$	$0.56^{+0.06}_{-0.05}$	4135^{+57}_{-70}	$-0.29^{+0.26}_{-0.16}$	199^{+25}_{-22}
201367065	11.4889966	-1.454787	$0.56^{+0.04}_{-0.04}$	$0.54^{+0.03}_{-0.04}$	3943^{+34}_{-43}	$-0.16^{+0.16}_{-0.15}$	45^{+3}_{-4}
201384232	11.8794840	-1.198477	$0.98^{+0.06}_{-0.07}$	$0.94^{+0.08}_{-0.07}$	5772^{+82}_{-80}	$-0.05^{+0.18}_{-0.20}$	335^{+30}_{-28}
201393098	11.1395847	-1.065755	$0.97^{+0.05}_{-0.06}$	$0.91^{+0.06}_{-0.06}$	5688^{+71}_{-67}	$-0.04^{+0.19}_{-0.19}$	405^{+29}_{-28}
201403446	11.6177563	-0.907261	$1.13^{+0.11}_{-0.14}$	$1.15^{+0.14}_{-0.17}$	6340^{+70}_{-68}	$-0.14^{+0.20}_{-0.34}$	372^{+53}_{-58}
201445392	11.3195777	-0.284375	$0.75^{+0.05}_{-0.07}$	$0.71^{+0.03}_{-0.07}$	4813^{+43}_{-44}	$-0.10^{+0.20}_{-0.26}$	386^{+21}_{-40}
201465501	11.7509645	0.005301	$0.32^{+0.09}_{-0.10}$	$0.32^{+0.08}_{-0.09}$	3453^{+53}_{-39}	$-0.18^{+0.19}_{-0.25}$	84^{+25}_{-25}
201505350	11.6640213	0.603575	$0.84^{+0.06}_{-0.07}$	$0.79^{+0.07}_{-0.10}$	5408^{+48}_{-50}	$-0.23^{+0.20}_{-0.38}$	280^{+26}_{-38}
201546283	11.4343443	1.230738	$0.86^{+0.05}_{-0.08}$	$0.80^{+0.04}_{-0.07}$	5290^{+48}_{-54}	$-0.09^{+0.21}_{-0.27}$	226^{+14}_{-22}
201549860	11.3402054	1.285956	$0.71^{+0.04}_{-0.05}$	$0.67^{+0.02}_{-0.04}$	4480^{+46}_{-46}	$-0.01^{+0.19}_{-0.18}$	242^{+12}_{-15}
201555883	11.7383960	1.375947	$0.61^{+0.03}_{-0.07}$	$0.59^{+0.02}_{-0.06}$	4404^{+42}_{-43}	$-0.39^{+0.13}_{-0.42}$	331^{+18}_{-39}
201565013	11.7994795	1.510249	$0.51^{+0.11}_{-0.04}$	$0.50^{+0.10}_{-0.04}$	3955^{+89}_{-51}	$-0.42^{+0.42}_{-0.15}$	501^{+121}_{-50}
201569483	11.1447533	1.577513	$0.83^{+0.04}_{-0.06}$	$0.77^{+0.04}_{-0.05}$	5111^{+54}_{-51}	$-0.04^{+0.19}_{-0.22}$	147^{+8}_{-31}
201577035	11.4747971	1.690636	$0.93^{+0.05}_{-0.06}$	$0.88^{+0.06}_{-0.05}$	5553^{+63}_{-63}	$-0.04^{+0.18}_{-0.18}$	256^{+19}_{-17}
201596316	11.2694668	1.986840	$0.83^{+0.07}_{-0.11}$	$0.77^{+0.05}_{-0.10}$	5254^{+46}_{-50}	$-0.16^{+0.25}_{-0.38}$	297^{+24}_{-41}
201613023	11.5461357	2.244884	$0.96^{+0.05}_{-0.08}$	$0.90^{+0.06}_{-0.08}$	5687^{+59}_{-60}	$-0.06^{+0.18}_{-0.26}$	259^{+20}_{-22}
201617985	11.9661106	2.321476	$0.50^{+0.04}_{-0.06}$	$0.48^{+0.03}_{-0.06}$	3681^{+43}_{-47}	$-0.04^{+0.15}_{-0.18}$	106^{+10}_{-15}
201629650	11.3437019	2.502696	$0.83^{+0.08}_{-0.07}$	$0.78^{+0.08}_{-0.06}$	5569^{+57}_{-56}	$-0.37^{+0.24}_{-0.26}$	288^{+33}_{-24}
201635569	11.8704684	2.594245	$0.50^{+0.08}_{-0.04}$	$0.48^{+0.08}_{-0.04}$	3829^{+74}_{-45}	$-0.31^{+0.30}_{-0.10}$	237^{+48}_{-24}
201649426	11.8156175	2.807619	$0.64^{+0.07}_{-0.05}$	$0.61^{+0.06}_{-0.05}$	4701^{+53}_{-47}	$-0.52^{+0.28}_{-0.35}$	183^{+20}_{-19}
201702477	11.6827196	3.681584	$0.92^{+0.05}_{-0.07}$	$0.87^{+0.06}_{-0.06}$	5551^{+72}_{-66}	$-0.08^{+0.17}_{-0.20}$	684^{+51}_{-52}
201736247	11.8740531	4.254747	$0.80^{+0.05}_{-0.07}$	$0.76^{+0.04}_{-0.07}$	5114^{+56}_{-57}	$-0.14^{+0.17}_{-0.26}$	486^{+29}_{-45}
201754305	11.6731505	4.557340	$0.67^{+0.06}_{-0.05}$	$0.64^{+0.05}_{-0.05}$	4717^{+40}_{-39}	$-0.35^{+0.21}_{-0.29}$	325^{+27}_{-25}
201779067	11.2361799	4.988131	$0.91^{+0.10}_{-0.06}$	$0.89^{+0.15}_{-0.08}$	6009^{+51}_{-53}	$-0.45^{+0.25}_{-0.22}$	180^{+33}_{-18}
201828749	11.7102895	5.894323	$0.85^{+0.07}_{-0.10}$	$0.80^{+0.07}_{-0.09}$	5437^{+56}_{-51}	$-0.23^{+0.24}_{-0.35}$	162^{+15}_{-20}
201855371	11.8886517	6.412261	$0.68^{+0.03}_{-0.05}$	$0.64^{+0.02}_{-0.04}$	4288^{+41}_{-41}	$0.01^{+0.19}_{-0.20}$	131^{+6}_{-9}
201912552 ¹	11.5040307	7.588391	$0.413^{+0.043}_{-0.043}$	$0.394^{+0.038}_{-0.038}$	3503^{+60}_{-60}	$0.09^{+0.09}_{-0.09}$	34^{+4}_{-4}
201929294	11.6437979	7.959611	$0.73^{+0.06}_{-0.09}$	$0.70^{+0.04}_{-0.08}$	4786^{+48}_{-53}	$-0.16^{+0.22}_{-0.34}$	197^{+13}_{-24}

NOTE. — These values and their uncertainties are derived from MCMC samplings and the numbers are computed as the 0.158, 0.500, and 0.842 posterior sample quantiles. The coordinates are retrieved directly from the EPIC.

¹ Parameters inferred from spectroscopic observations.

TABLE 3
PLANET PROPERTIES FOR ALL OBJECTS OF INTEREST

Candidate	Period (days)	Epoch (BJD-2456808)	Radius (R_{\oplus})	a/R_*	a (AU)	T_{eq} (K)	Disposition
201208431.01	10.00411 \pm 0.00163	7.5198 \pm 0.0085	2.33 \pm 0.26	27.68 \pm 0.94	0.0780 \pm 0.0016	562 \pm 14	Planet
201257461.01	50.26759 \pm 0.00743	20.3803 \pm 0.0185	13.55 \pm 8.55	79.73 \pm 4.60	0.2323 \pm 0.0066	381 \pm 13	FP
201295312.01	5.65621 \pm 0.00075	3.7229 \pm 0.0114	1.95 \pm 0.26	13.43 \pm 1.16	0.0629 \pm 0.0015	1150 \pm 55	Candidate
201338508.01	10.93271 \pm 0.00200	6.5961 \pm 0.0079	2.14 \pm 0.37	30.90 \pm 1.66	0.0804 \pm 0.0024	526 \pm 21	Planet
201338508.02	5.73501 \pm 0.00058	0.8636 \pm 0.0061	2.03 \pm 0.24	20.10 \pm 1.08	0.0523 \pm 0.0016	652 \pm 26	Planet
201367065.01	10.05429 \pm 0.00032	5.4184 \pm 0.0019	2.12 \pm 0.22	30.24 \pm 1.59	0.0749 \pm 0.0020	507 \pm 17	Planet
201367065.02	24.64682 \pm 0.00149	4.2766 \pm 0.0031	1.59 \pm 0.15	54.98 \pm 2.89	0.1361 \pm 0.0036	376 \pm 13	Planet
201384232.01	30.93716 \pm 0.00428	19.5044 \pm 0.0056	2.68 \pm 0.31	44.08 \pm 3.92	0.1911 \pm 0.0048	616 \pm 31	Planet
201393098.01	28.68077 \pm 0.01250	16.6201 \pm 0.0225	2.34 \pm 0.48	43.14 \pm 3.07	0.1808 \pm 0.0041	614 \pm 25	Planet
201403446.01	19.15379 \pm 0.00565	7.3425 \pm 0.0135	1.91 \pm 0.35	28.06 \pm 3.72	0.1447 \pm 0.0052	852 \pm 56	Candidate
201445392.01	10.35262 \pm 0.00116	5.6113 \pm 0.0048	2.74 \pm 0.51	26.35 \pm 1.35	0.0837 \pm 0.0023	663 \pm 20	Candidate
201445392.02	5.06442 \pm 0.00066	5.0675 \pm 0.0067	2.17 \pm 0.39	16.36 \pm 0.84	0.0520 \pm 0.0014	841 \pm 26	Candidate
201465501.01	18.44878 \pm 0.00143	14.6719 \pm 0.0032	1.74 \pm 0.63	71.01 \pm 14.29	0.0885 \pm 0.0104	293 \pm 30	Candidate
201505350.01	11.90699 \pm 0.00035	9.2850 \pm 0.0080	4.51 \pm 0.66	26.15 \pm 3.14	0.0961 \pm 0.0026	752 \pm 45	Planet
201505350.02	7.91933 \pm 0.00007	5.3837 \pm 0.0009	6.37 \pm 0.85	19.93 \pm 2.40	0.0733 \pm 0.0020	861 \pm 52	Planet
201546283.01	6.77133 \pm 0.00011	4.8450 \pm 0.0015	4.11 \pm 0.38	18.38 \pm 1.12	0.0658 \pm 0.0018	873 \pm 28	Candidate
201549860.01	5.60822 \pm 0.00057	4.1193 \pm 0.0049	2.13 \pm 0.44	17.83 \pm 0.61	0.0548 \pm 0.0012	750 \pm 17	Candidate
201555883.01	5.79658 \pm 0.00023	5.3179 \pm 0.0027	3.75 \pm 0.56	20.10 \pm 1.06	0.0530 \pm 0.0015	694 \pm 24	FP
201565013.01	8.63811 \pm 0.00023	3.4285 \pm 0.0016	12.15 \pm 3.91	28.87 \pm 2.84	0.0660 \pm 0.0033	523 \pm 40	Candidate
201569483.01	5.79690 \pm 0.00001	5.3127 \pm 0.0001	34.10 \pm 5.09	16.89 \pm 0.85	0.0588 \pm 0.0015	880 \pm 25	FP
201577035.01	19.30622 \pm 0.00136	11.5785 \pm 0.0031	3.58 \pm 0.61	35.11 \pm 5.34	0.1365 \pm 0.0035	668 \pm 49	Planet
201596316.01	39.84348 \pm 0.01392	21.8566 \pm 0.0096	2.23 \pm 0.38	61.36 \pm 4.19	0.2126 \pm 0.0072	475 \pm 19	Candidate
201613023.01	8.28186 \pm 0.00060	7.3738 \pm 0.0061	2.03 \pm 0.24	18.99 \pm 1.60	0.0786 \pm 0.0020	925 \pm 38	Planet
201617985.01	7.28210 \pm 0.00076	4.6341 \pm 0.0046	1.78 \pm 0.58	27.38 \pm 2.14	0.0573 \pm 0.0022	497 \pm 24	Candidate
201629650.01	40.04833 \pm 0.02111	4.5343 \pm 0.0172	2.12 \pm 0.52	59.20 \pm 4.08	0.2153 \pm 0.0059	513 \pm 19	Planet
201635569.01	8.36807 \pm 0.00019	3.4511 \pm 0.0017	5.13 \pm 0.77	29.29 \pm 2.48	0.0636 \pm 0.0025	502 \pm 27	Candidate
201649426.01	27.77044 \pm 0.00006	13.3479 \pm 0.0002	30.03 \pm 5.78	56.87 \pm 4.97	0.1523 \pm 0.0063	440 \pm 22	FP
201702477.01	40.73649 \pm 0.00245	3.5451 \pm 0.0026	7.66 \pm 0.81	55.99 \pm 3.67	0.2239 \pm 0.0051	526 \pm 19	Planet
201736247.01	11.81037 \pm 0.00170	3.8492 \pm 0.0081	2.82 \pm 0.32	27.44 \pm 1.42	0.0936 \pm 0.0023	690 \pm 21	Planet
201754305.01	19.07246 \pm 0.00519	1.4889 \pm 0.0148	2.21 \pm 0.84	41.60 \pm 2.07	0.1219 \pm 0.0035	517 \pm 16	Planet
201754305.02	7.62016 \pm 0.00103	3.6811 \pm 0.0057	2.18 \pm 1.04	22.57 \pm 1.12	0.0661 \pm 0.0019	702 \pm 22	Planet
201779067.01	27.24292 \pm 0.00013	12.2594 \pm 0.0004	38.51 \pm 8.27	33.03 \pm 5.39	0.1784 \pm 0.0053	746 \pm 58	FP
201828749.01	33.50924 \pm 0.00228	5.1556 \pm 0.0042	2.47 \pm 0.81	57.87 \pm 18.68	0.1903 \pm 0.0066	519 \pm 62	Candidate
201855371.01	17.97149 \pm 0.00164	9.9414 \pm 0.0035	2.19 \pm 0.23	40.14 \pm 1.60	0.1169 \pm 0.0028	478 \pm 13	Planet
201912552.01 ¹	32.94139 \pm 0.00292	28.1877 \pm 0.0036	2.24 \pm 0.25	84.27 \pm 9.54	0.1491 \pm 0.0053	271 \pm 16	Planet
201929294.01	5.00842 \pm 0.00006	4.5719 \pm 0.0014	8.62 \pm 0.72	16.33 \pm 0.92	0.0513 \pm 0.0016	838 \pm 29	FP

NOTE. — These values and uncertainties are given by the mean and standard deviation of MCMC posterior samplings.

¹ Parameters inferred from spectroscopic observations.

TABLE 4
FALSE POSITIVE PROBABILITY CALCULATION RESULTS

Candidate	$\delta_{\text{sec,max}}$ [ppt] ¹	AO? ²	Pr _{EB}	Pr _{BEB}	Pr _{HEB}	f_p ³	FPP	Disposition
201208431.01	0.51	-	$< 10^{-4}$	$< 10^{-4}$	7.0×10^{-4}	0.21	7.0×10^{-4}	Planet
201257461.01	0.59	-	8.8×10^{-3}	0.940	0.051	0.17	1.000	FP
201295312.01	0.04	Y	$< 10^{-4}$	$< 10^{-4}$	$< 10^{-4}$	0.21	$< 10^{-4}$	Candidate ^a
201338508.01	0.63	-	$< 10^{-4}$	$< 10^{-4}$	3.2×10^{-3}	0.21	3.2×10^{-3}	Planet
201338508.02	0.33	-	$< 10^{-4}$	$< 10^{-4}$	1.8×10^{-4}	0.22	1.8×10^{-4}	Planet
201367065.01	0.15	-	0.717	$< 10^{-4}$	0.044	0.07	0.761	Planet ^c
201367065.02	0.67	-	3.2×10^{-3}	$< 10^{-4}$	4.2×10^{-3}	0.17	7.4×10^{-3}	Planet ^c
201384232.01	0.44	-	1.2×10^{-4}	$< 10^{-4}$	$< 10^{-4}$	0.16	1.4×10^{-4}	Planet
201393098.01	0.52	-	1.6×10^{-3}	$< 10^{-4}$	5.5×10^{-4}	0.19	2.2×10^{-3}	Planet
201403446.01	0.18	Y	$< 10^{-4}$	$< 10^{-4}$	$< 10^{-4}$	0.22	$< 10^{-4}$	Candidate ^a
201445392.01	0.26	-	1.3×10^{-3}	$< 10^{-4}$	0.012	0.19	0.013	Candidate
201445392.02	0.18	-	0.023	$< 10^{-4}$	0.254	0.21	0.277	Candidate
201465501.01	0.68	-	0.491	0.022	9.1×10^{-3}	0.20	0.522	Candidate
201505350.01	2.69	-	0.583	$< 10^{-4}$	0.024	0.07	0.607	Planet ^d
201505350.02	0.70	-	0.034	$< 10^{-4}$	2.3×10^{-4}	0.07	0.034	Planet ^d
201546283.01	0.15	-	$< 10^{-4}$	$< 10^{-4}$	$< 10^{-4}$	0.06	1.1×10^{-4}	Candidate ^a
201549860.01	0.18	-	7.5×10^{-3}	0.014	0.011	0.22	0.032	Candidate
201555883.01	0.94	-	$< 10^{-4}$	$< 10^{-4}$	3.6×10^{-3}	0.10	3.6×10^{-3}	FP ^b
201565013.01	1.69	-	0.460	0.391	0.035	0.06	0.887	Candidate
201569483.01	2.06	-	0.437	0.562	$< 10^{-4}$	0.00	0.999	FP
201577035.01	0.14	Y	3.0×10^{-4}	$< 10^{-4}$	$< 10^{-4}$	0.07	3.6×10^{-4}	Planet
201596316.01	0.45	-	0.017	$< 10^{-4}$	3.4×10^{-4}	0.20	0.017	Candidate
201613023.01	0.08	Y	9.8×10^{-4}	$< 10^{-4}$	$< 10^{-4}$	0.20	9.8×10^{-4}	Planet
201617985.01	0.27	-	0.166	$< 10^{-4}$	0.053	0.19	0.219	Candidate
201629650.01	0.43	-	1.5×10^{-3}	$< 10^{-4}$	2.6×10^{-4}	0.18	1.8×10^{-3}	Planet
201635569.01	0.79	-	$< 10^{-4}$	$< 10^{-4}$	0.043	0.06	0.043	Candidate
201649426.01	3.10	-	0.856	0.142	1.6×10^{-4}	0.00	0.998	FP
201702477.01	0.70	-	$< 10^{-4}$	$< 10^{-4}$	4.0×10^{-3}	0.06	4.0×10^{-3}	Planet
201736247.01	0.42	-	$< 10^{-4}$	$< 10^{-4}$	4.6×10^{-4}	0.18	4.9×10^{-4}	Planet
201754305.01	0.65	-	2.5×10^{-3}	$< 10^{-4}$	3.2×10^{-3}	0.21	5.7×10^{-3}	Planet
201754305.02	0.38	-	1.9×10^{-3}	$< 10^{-4}$	1.7×10^{-3}	0.22	3.6×10^{-3}	Planet
201779067.01	1.97	-	0.935	0.063	3.2×10^{-4}	0.00	0.998	FP
201828749.01	0.39	Y	2.6×10^{-3}	$< 10^{-4}$	$< 10^{-4}$	0.17	2.6×10^{-3}	Candidate ^a
201855371.01	0.62	-	$< 10^{-4}$	$< 10^{-4}$	$< 10^{-4}$	0.22	$< 10^{-4}$	Planet
201912552.01	0.47	Y	$< 10^{-4}$	$< 10^{-4}$	$< 10^{-4}$	0.21	$< 10^{-4}$	Planet
201929294.01	3.12	-	$< 10^{-4}$	$< 10^{-4}$	2.8×10^{-4}	0.07	2.9×10^{-4}	FP ^b

NOTE. — Results of the **vespa** astrophysical false positive probability calculations for all candidates. Likely false positives (FPP > 0.9, or otherwise designated) are marked in red. Candidates are declared to be validated planets if FPP < 0.01. EB, BEB, and HEB refer to the three considered astrophysical false positive scenarios, and the relative probability of each is listed in the appropriate column. Planets previously identified in the literature are marked as planets even if FPP is not below 1% threshold.

¹ Maximum depth of potential secondary eclipse signal.

² Whether adaptive optics observation is presented in this paper.

³ Integrated planet occurrence rate assumed between $0.7\times$ and $1.3\times$ the candidate radius

^a Despite low FPP, returned to candidate status out of abundance of caution due to secondary star detection within or near photometric aperture.

^b Declared a false positive due to noise modeling systematics (see §5.2).

^c Identified as planets by Crossfield et al. (2015). High FPP because of overlapping transit events affecting the transit shape.

^d Identified as planets by Armstrong et al. (2015b).

TABLE 5
DETECTED COMPANIONS TO CANDIDATE HOST STARS

Primary	Aperture (arcsec)	RA (J2000)	Dec (J2000)	Detection	Separation (arcsec)	Δr (mag)	Max Depth (ppt)	Observed Depth (ppt)
201208431	15.9	174.748988	-3.902146	SDSS	17.25 ± 0.15^1	5.90 ± 0.12	5.6	1.20
201257461	19.9	178.164376	-3.093431	SDSS	12.91 ± 0.18^1	5.04 ± 0.03	4.8	30.54
201295312	11.9	174.010158	-2.522528	SDSS/AO	8.12 ± 0.09^1	7.10 ± 0.10	0.8	0.30
201338508	15.9	169.308176	-1.873647	SDSS	22.92 ± 0.07^1	4.35 ± 0.03	9.1	1.07
201367065	19.9							1.26
201384232	13.9	178.195303	-1.192501	SDSS	24.14 ± 0.06^1	5.93 ± 0.03	2.1	0.68
201393098	15.9							0.53
201403446	15.9	174.267663	-0.909645	SDSS	9.78 ± 0.14^1	4.56 ± 0.08	7.5	0.23
201445392	13.9							0.78
201465501	11.9							2.83
201505350	19.9							2.64
201546283	17.9	171.515265	1.229950	SDSS/AO	2.98 ± 0.05^1	5.87 ± 0.06	2.3	2.33
201549860	13.9	170.097556	1.288007	SDSS	21.21 ± 0.05^1	2.26 ± 0.03	62.3	0.80
201555883	10.0							3.50
201565013	10.0							45.8
201569483	19.9							160
201577035	19.9	172.118116	1.687798	SDSS	17.19 ± 0.12^1	5.40 ± 0.03	3.5	1.44
201596316	15.9							0.70
201613023	19.9							0.42
201617985	15.9							1.10
201629650	15.9	170.158905	2.502107	SDSS	12.30 ± 0.14^1	5.98 ± 0.06	2.0	0.58
201635569	11.9							9.43
201649426	19.9							216
201702477	10.0	175.238916	3.678764	SDSS	12.15 ± 0.12^1	4.65 ± 0.09	6.9	6.70
201736247	13.9							1.21
201754305	11.9							0.80
201779067	19.9							84.9
201828749	11.9	175.645724	5.894714	AO	2.46 ± 0.04^1	2.0 ± 0.1^3	137	0.76
201855371	19.9							0.99
201912552	13.9							2.85
201929294	19.9							13.56

¹ Separation from AO imaging

² Separation from SDSS photometry

³ Δr inferred from JHK relative photometry.